Volume 11 | Number 37 | 7 October 2019 | Pages 17123–17520

Nanoscale

rsc.li/nanoscale

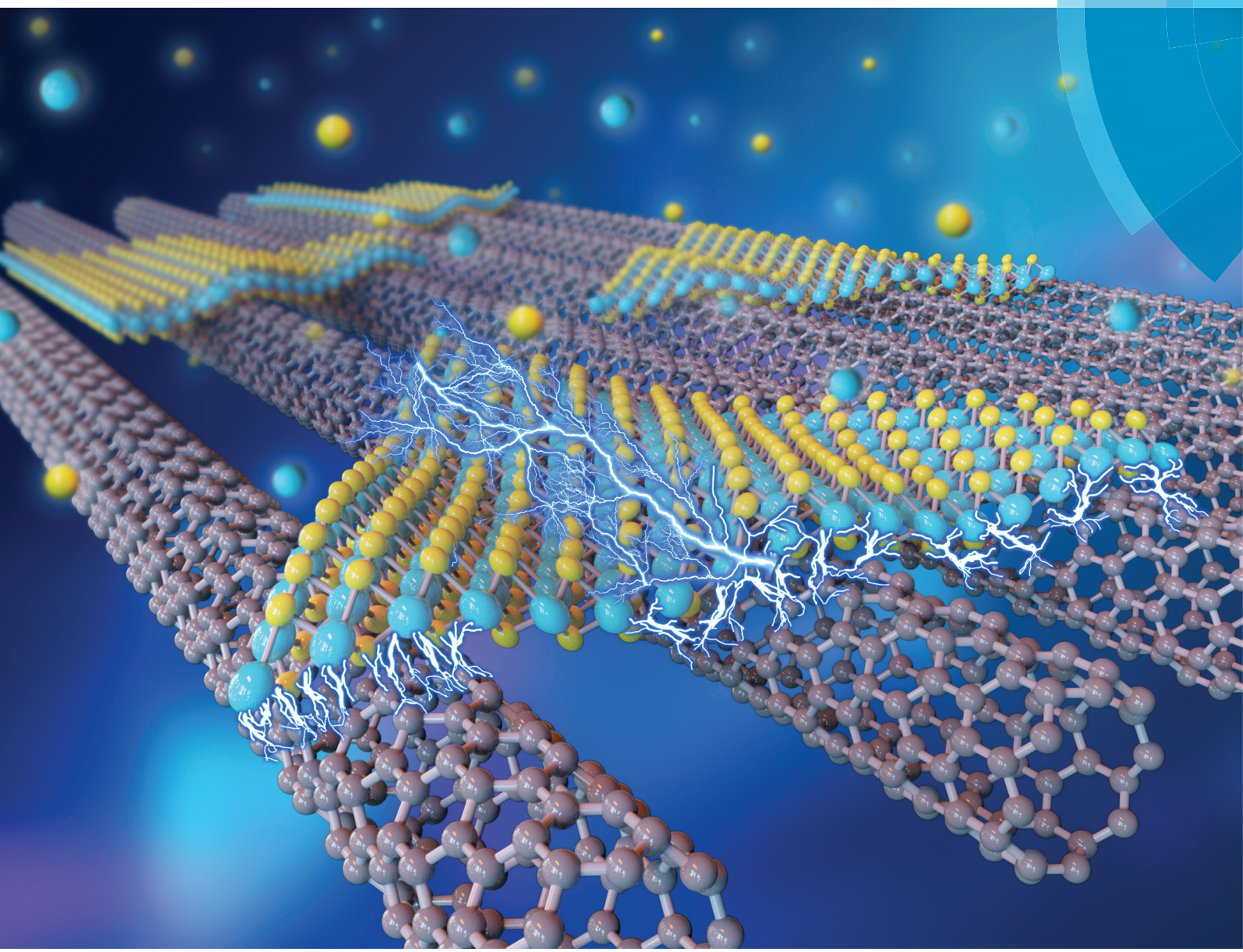

ISSN 2040-3372

ROYAL SOCIETY OF CHEMISTRY | Celebrating IYPT 2019

COMMUNICATION

Kaihui Liu *et al.*

Strong-coupled hybrid structure of carbon nanotube and MoS_2 monolayer with ultrafast interfacial charge transfer

NCNST

Nanoscale

COMMUNICATION

Check for updates

Cite this: *Nanoscale*, 2019, **11**, 17195

Received 5th June 2019,
Accepted 9th July 2019

DOI: 10.1039/c9nr04791c

rsc.li/nanoscale

Strong-coupled hybrid structure of carbon nanotube and MoS_2 monolayer with ultrafast interfacial charge transfer†

Can Liu, ‡[a] Hao Hong,‡[a] Qinghe Wang,[a] Ping Liu,[b] Yonggang Zuo,[c] Jing Liang,[a] Yang Cheng,[a] Xu Zhou,[a] Jinhuan Wang,[d] Yun Zhao, [d] Jie Xiong, [e] Bin Xiang, [b] Jin Zhang [f] and Kaihui Liu *[a]

Hybrid structures assembled by van der Waals (vdW) interactions greatly expand the conventional material platforms, as there is no constraint of lattice matching in the materials design. However, a general challenge lies in the controllable assembly of 1D–2D hybrids with strong-coupled interfaces, because the interaction area is very small and is easily disturbed by exotic molecules. Here, we report the direct construction of 1D carbon nanotube-2D MoS_2 monolayer hybrids with strong interfacial coupling using a sequential chemical vapour deposition growth method. The strong mechanical and electronic couplings between the nanotubes and MoS_2 are unambiguously illustrated from the Raman-mode frequency shift and ultrafast interfacial charge transfer (~100 fs). The findings in this work will boost the mass fabrication of 1D–2D vdW hybrid materials with controllable interfacial geometry and coupling strength, and pave the way for their future applications in electronics, optoelectronics and photovoltaics.

Introduction

The free assembly of low-dimensional materials by van der Waals (vdW) interactions opens up a new era in materials research since there is no constraint in lattice matching as in conventional materials design and the resulting materials platforms become extremely rich.[1–4] These artificial vdW heterostructures possess distinct properties to those of their individual components and exhibit great potential in the application of next-generation nanoelectronics, optoelectronics and photovoltaics.[5–7] Currently, the prevailing building blocks for vdW hybrids are mostly limited to two-dimensional (2D) materials, mainly due to the easy fabrication of a 2D interface with controlled geometry and coupling strength *via* either exfoliation-transfer,[8] solution stacking[9,10] or direct growth techniques.[11–14] Actually, there are other lower-dimensional materials, such as the very rich one-dimensional (1D) materials, that can be assembled with 2D materials, which is believed to further expand the materials platform of vdW hybrids and promote properties and applications beyond those of 2D hybrids only. For example, previous works, although very few, on 1D–2D hybrid structures have already demonstrated superior device performances, such as nanoscale resolution in a vertical point heterostructure,[15] wide gate tunability in a p–n heterojunction,[16] and enhanced performances in lithium-ion batteries[17–19] and hydrogen evolution reaction.[20,21] Despite these extraordinary properties of 1D–2D hybrids, the key interfacial geometry and coupling strength has not been controlled purposely. Therefore, there is a great demand to develop a facile and efficient method to produce 1D–2D hybrid structures with a controlled interface.

In principle, a 1D–2D hybrid structure can be easily obtained by directly stacking two components together. Unfortunately, uniform and strong interfacial coupling between 1D and 2D components is not naturally guaranteed, because the interaction area is very small, at only a nanometer in width, and is easily disturbed by exotic molecules, which is much more difficult to control than that in 2D–2D hybrids that have a larger interaction area and cleaner interface. Therefore, one needs to develop new strategies to precisely control the 1D–2D interface during hybrid component assembly.

Recently, a sequential chemical vapour deposition (CVD) method was developed to directly grow 2D hybrids (both in-

[a]*State Key Laboratory for Mesoscopic Physics, Collaborative Innovation Center of Quantum Matter, School of Physics, Academy for Advanced Interdisciplinary Studies, Peking University, Beijing 100871, China. E-mail: khliu@pku.edu.cn*
[b]*Department of Materials Science & Engineering, University of Science and Technology of China, Hefei, Anhui 230026, China*
[c]*Beijing National Laboratory for Condensed Matter Physics, Institute of Physics, Chinese Academy of Sciences, Beijing 100080, China*
[d]*School of Chemistry and Chemical Engineering, Beijing Institute of Technology, Beijing 100081, China*
[e]*State Key Laboratory of Electronic Thin Films and Integrated Devices, University of Electronic Science and Technology of China, Chengdu 610054, China*
[f]*Center for Nanochemistry, College of Chemistry and Molecular Engineering, Peking University, Beijing 100871, China*

†Electronic supplementary information (ESI) available: Measurement of AFM, SEM characterization and stacking geometries. See DOI: 10.1039/c9nr04791c

‡These authors contributed equally to this research work.

plane and out-of-plane stacked) with high-stacking-quality interfaces.[12–14] The basic idea is to control the feedstock and growth conditions between the growth process of the two hybrid components. In this work, we employed and developed the sequential CVD method to construct 1D carbon nanotube-2D MoS_2 monolayer hybrids with strong interfacial coupling. The successful synthesis can be attributed to two key design controls: (i) hydrogen annealing between the two-component growth to eliminate amorphous contamination and ensure a clean interface and (ii) growth of MoS_2 after the nanotubes to make the 2D structure spread over the 1D structure and form a large interaction area. A clean interface with large interaction area leads to strong mechanical and electronic interfacial coupling, as illustrated by the phonon energy modulation and ultrafast interlayer charge transfer dynamics. The findings in this work should shed light on the mass fabrication of broad 1D–2D vdW hybrid materials with controllable interfacial geometry and coupling strength, and facilitate their future applications in electronic, optoelectronic and photovoltaic devices with reduced size and enhanced performance.

Results and discussion

To construct a hybrid structure of 1D nanotubes covered by a 2D MoS_2 monolayer, we designed our sequential CVD procedure, growing the nanotubes before MoS_2 (Fig. 1a). After using typical growth conditions for the nanotubes and MoS_2 (see the Methods section for growth details), scanning electron microscopy (SEM) was carried out and the SEM image shows that MoS_2 triangular domains prefer to nucleate on nanotubes rather than on bare substrate (Fig. 1b). Further statistical data on the relative angle θ between the MoS_2 triangle and the nanotube axis T_{NT} along one individual nanotube reveals that there is no observable preference for in-plane MoS_2 rotation (Fig. 1c and d). In principle, one may expect some dominant MoS_2 rotation angles, as observed in 2D MoS_2-graphene hybrid materials with a clean interface.[22–24] This random angle distribution of MoS_2 indicates that the 1D–2D interface between the nanotubes and MoS_2 is not clean. Indeed, the optical images for longer MoS_2 growth time show obvious multi-layers of MoS_2 along the nanotube axis, which gives a higher contrast than that away from the nanotubes (Fig. 1e). This multi-layered MoS_2 structure is further demonstrated by the much larger height in the atomic force microscopy (AFM) image (ESI Fig. S1†), greatly reduced emission intensity in the photoluminescence spectrum (Fig. 1f), and larger frequency difference between the E_{2g} and A_{1g} modes in the Raman spectrum of MoS_2 in the hybrid region (Fig. 1g). The formation of a multi-layer of MoS_2 on the nanotubes is believed to originate from the dangling bonds of amorphous carbon on the nanotubes during the growth, which act as very active nucleation centres for MoS_2 growth.[25] Obviously, normal sequential growth cannot produce nanotube-MoS_2 hybrids with a clean interface due to the existence of possible amorphous carbon on the nanotube surface.

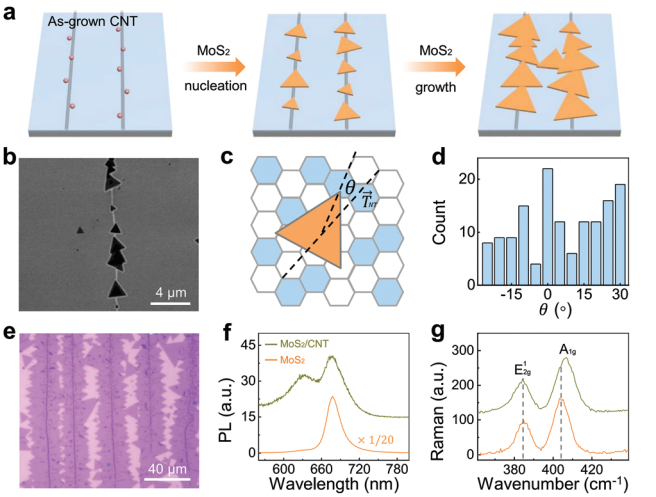

Fig. 1 Carbon nanotube (CNT)-MoS_2 hybrids with a dirty interface. (a) Schematic illustration of the designed sequential CVD procedure for growing MoS_2 after the nanotubes. (b) SEM image of MoS_2 triangular domains nucleating on an individual nanotube. MoS_2 nuclei on a nanotube show a higher density than on bare substrate. (c) Definition of the relative angle θ between the MoS_2 triangles and nanotube axis T_{NT}. (d) Statistics of θ on an individual nanotube. The random distribution indicates that there is no observable confinement for the in-plane MoS_2 rotation. (e) Optical image for a longer MoS_2 growth time. The profile of nanotubes is visible due to the enhanced contrast of multi-layered MoS_2 along the nanotubes. (f and g) Photoluminescence and Raman spectra of MoS_2 along an as-grown nanotube and those on bare substrate. Both the strongly decreased photoluminescence intensity (f) and the wider peak spacing between E_{2g} and A_{1g} mode (g) show the multilayer characteristics of MoS_2 on the nanotubes.

To obtain a clean interface in the nanotube-MoS_2 hybrid structure, the key issue is to have a clean nanotube surface before MoS_2 growth. In the nanotube growth field, it is known that hydrogen annealing at a proper temperature can etch the amorphous carbon away but keep the nanotubes intact (amorphous carbon is more reactive than graphitic nanotubes).[26–30] In our experiment, we added a hydrogen annealing process at 700 °C for 15 min after nanotube growth but before MoS_2 growth (Fig. 2a). After the same procedure of MoS_2 growth as that in normal growth without hydrogen annealing, an entirely different growth result occurred: MoS_2 domains nucleated randomly on the whole substrate rather than on the nanotubes (Fig. 2b); the nanotube outlines cannot be seen in the optical images anymore but a uniform MoS_2 monolayer contrast on and off the nanotube (ESI Fig. S2†), no photoluminescence decrease in the MoS_2 on the nanotube region (Fig. 2c), and a uniform frequency difference of 19 cm^{-1} between the E_{2g} and A_{1g} modes of monolayer MoS_2 (Fig. 2d) can be observed. All of the above characteristic features illustrate clean nanotube-MoS_2 monolayer hybrid structures without the formation of multi-layer MoS_2 at the interface.

In principle, there are two possible stacking geometries in nanotube-MoS_2 hybrids, *i.e.* MoS_2 grows over the nanotube or the nanotubes sit on MoS_2, and the first geometry is preferred as it presents a larger interaction area with strong interfacial

This journal is © The Royal Society of Chemistry 2019

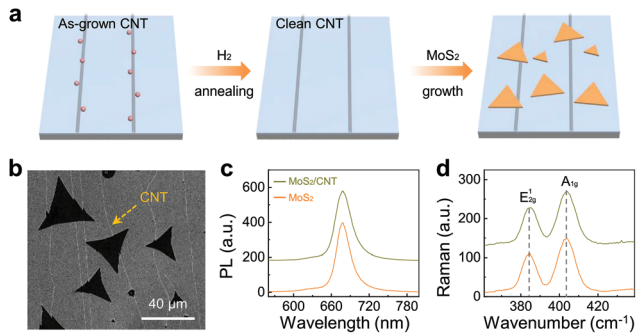

Fig. 2 Carbon nanotube-MoS_2 hybrids with a clean interface. (a) Schematic illustration of the optimized sequential CVD process. By annealing the nanotubes before the growth of MoS_2, amorphous carbon can be etched away, and a clean interface is guaranteed. (b) SEM image of the randomly nucleated MoS_2 domains on the whole substrate. Clean nanotubes do not act as nucleation centres. (c) Photoluminescence spectra of MoS_2 on and off the nanotube. (d) The Raman spectra of MoS_2 display a uniform frequency difference of 19 cm^{-1} between the E_{2g} and A_{1g} modes. All signatures in (c and d) illustrate that the MoS_2 samples are homogeneous monolayers.

coupling (Fig. 3a). To verify the vertical stacking relationship between the nanotubes and MoS_2, AFM was first carried out to analyse the cross-sectional profile across the nanotubes. Representative AFM images of the same nanotube on bare substrate and hybridized with a MoS_2 monolayer are presented in Fig. 3b. The height of the two curves are almost the same (~1.9 nm), while in the nanotube-MoS_2 region, the full width at half maximum intensity (16.0 nm) is greater than in the bare nanotube region (11.0 nm) (Fig. 3c), which is a strong indication that the MoS_2 is growing over the nanotube. However, if the nanotube is sitting on MoS_2, the measured AFM width across a nanotube should be very similar (ESI Fig. S3†). We further employed a water washing method to verify the interfacial climbing-over geometry in the nanotube-MoS_2 hybrids. As pure MoS_2 can be easily washed out by water immersion but nanotubes cannot (ESI Fig. S4†), one can determine whether the nanotubes are on or under MoS_2 by observing whether the nanotubes are washed away with MoS_2 or not. If the nanotubes are washed away, the nanotubes are sitting on the MoS_2 and *vice versa*. The results show that after soaking the hybrid sample in water and taking it out, the MoS_2 domains are removed but the nanotubes remain (Fig. 3d and e), which confirms the climbing-over geometry between the nanotubes and MoS_2 at the interface.

This climbing-over geometry is against common sense. As a nanotube is typically 2 nm in diameter and a MoS_2 monolayer is only ~0.7 nm in thickness, during the post-growth of MoS_2, one would expect MoS_2 to grow underneath the nanotubes instead of climbing over them. This climbing behaviour of MoS_2 on the nanotubes should be attributed to the interaction strength difference between the nanotubes and MoS_2 to the substrate. From the water washing phenomenon, it has already been revealed that the nanotube-substrate interaction is much stronger than the MoS_2-subsrate one, so during MoS_2 growth on the nanotubes, it takes less energy for MoS_2 to climb on the nanotubes than push the nanotubes up away from the substrate (Fig. 3a). This growth mechanism is also supported by our observation that the MoS_2 forms a discontinuous edge at

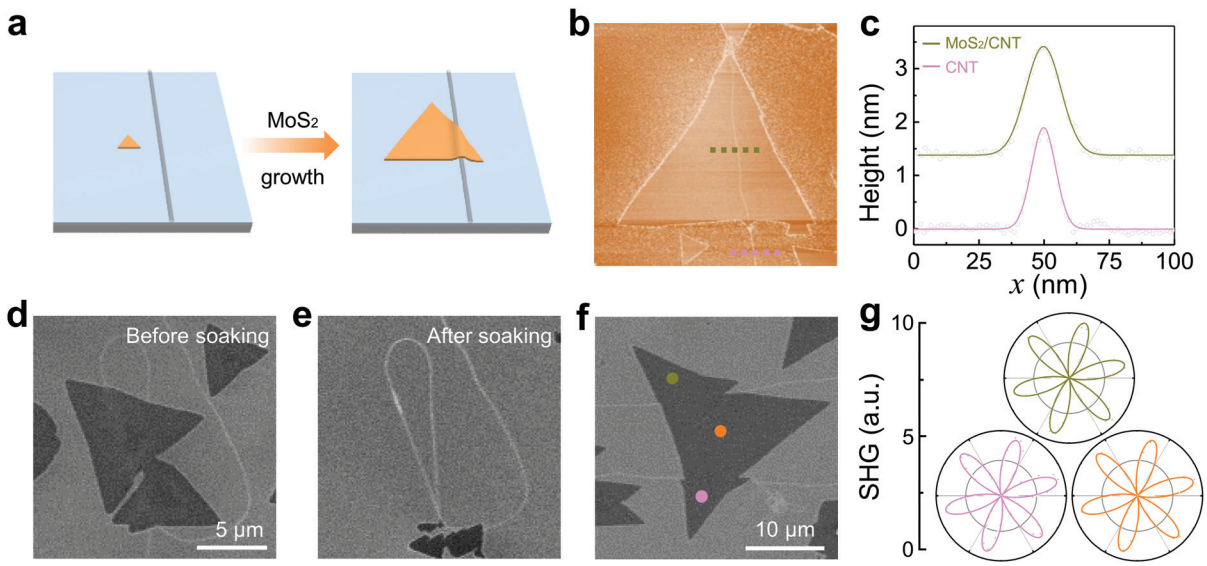

Fig. 3 Carbon nanotube-MoS_2 hybrids with large interaction area. (a) Schematic illustration of the process of MoS_2 climbing over one nanotube. (b) AFM image of the same nanotube on bare substrate and hybridized with a MoS_2 monolayer. (c) AFM cross-sectional profiles along the line labelled in (b). The height of the two curves are almost the same (~1.9 nm), while the nanotube-MoS_2 region has a larger full width at half maximum intensity (16.0 nm) than the bare nanotube region (11.0 nm). (d and e) SEM images of the nanotube-MoS_2 hybrid structure before (d) and after (e) soaking in water. (f) SEM image of a MoS_2 monolayer grown across nanotubes and discontinuous edges are formed at two sides of the nanotubes. (g) Polarized SHG patterns at different positions labelled in (f), indicating that the whole MoS_2 domain is still a single crystal.

two sides of the nanotubes. As the MoS_2 climbing consumes some energy (MoS_2 will bend to increase the strain energy), not all of the MoS_2 can climb over the nanotubes at the same time, leading to unequal length (Fig. 3f). However, the whole domain is still a single crystal, as proved by the same polarized second-harmonic generation (SHG) pattern at different positions (Fig. 3g). This specific climbing growth behaviour of MoS_2 leads to a larger interaction area between the nanotubes and MoS_2 at the interface.

The clean interface with large interaction area naturally results in strong interfacial coupling in nanotube-MoS_2 hybrids both mechanically and electronically. This strong coupling was first demonstrated in the vibration frequency shift of the specific Raman modes of the nanotubes. The nanotube radial breathing mode (RBM), which is the in-phase collective motion of atoms along the radial direction and a characteristic Raman mode of 1D materials, is hardened by ~1 cm^{-1} with MoS_2 coverage (Fig. 4a and b). This blue-shift can be attributed to the strong interlayer mechanical coupling between the nanotubes and MoS_2 (mechanical coupling enhances the effective force constant of RBM vibrations).[31] The nanotube G mode is sensitive to carrier doping and its frequency is therefore an indicator of interlayer charge transfer.[32] From the band alignment configuration, the as-prepared nanotube-MoS_2 hybrids naturally form a p–n junction, as pristine nanotubes are p-type, while MoS_2 are n-type (Fig. 4c).[16] The electrons will transfer from the MoS_2 to the nanotubes through the strong electronically coupled interface. As a consequence, the G-mode Raman frequency of the nanotubes red-shifts by ~2 cm^{-1} (Fig. 4d) (the electron transfer makes the original p-type nanotubes more neutral).[32] It is worth noting that these Raman shifts cannot be detected for MoS_2 since the 2D excited area (laser spot) is two orders of magnitude larger than that of the 1D hybrid area.

The strong interfacial electronic coupling between the nanotubes and MoS_2 can also be demonstrated from their ultrafast charge transfer dynamics.[33,34] We performed ultrafast pump–probe spectroscopy to capture this process in a temporal profile with a pulse width of 100 fs. Since the single-tube signal is too weak to be detected in the ultrafast spectroscopy, we grew MoS_2 on aligned dense nanotube arrays to enhance the signal (a laser spot can cover many nanotube-MoS_2 samples). Using a pump fluence of 12 μJ cm^{-2}, we resonantly pumped MoS_2 at 680 nm and selectively probed at a longer wavelength of 820 nm (Fig. 4e). Time-resolved transient absorption (TA) signals of the pristine nanotube arrays, pristine MoS_2 and their corresponding hybrids are shown in Fig. 4f. The TA signals of the nanotubes and MoS_2 are consistent with those in previous reports and the understanding is that the nanotube signal rises up quickly and then decays to

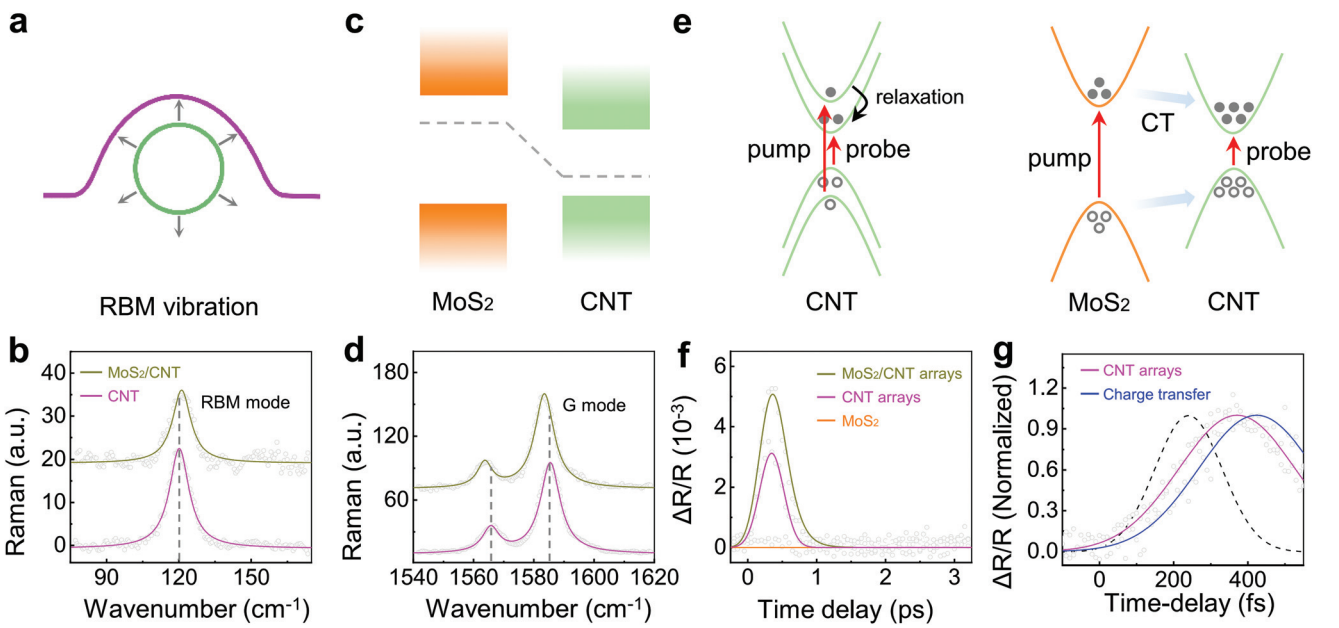

Fig. 4 Strong interlayer coupling and ultrafast charge transfer at a clean interface. (a and b) RBM Raman spectra of nanotube and nanotube-MoS_2 hybrid structures. The covering of MoS_2 hardens the RBM peak of the nanotubes by ~1 cm^{-1}, indicating strong interlayer mechanical coupling. (c) Schematic illustration of the formed p–n junction with n-type MoS_2 covering the p-type nanotubes. (d) G-mode Raman spectra of nanotubes with and without MoS_2 coverage. The formed p–n junction allows electrons transfer from MoS_2 to the nanotubes and the G peak position red-shifts by ~2 cm^{-1}. (e) Scheme of the carrier dynamics and interlayer charge transfer after photoexcitation in aligned dense nanotube arrays and nanotube array-MoS_2 hybrid structures, respectively. (f) Evolution of the TA signal of pristine nanotube arrays, pristine MoS_2 and their hybrid structures. With MoS_2 coverage above, the signal of the nanotubes is enhanced due to interlayer charge transfer. (g) The charge transfer signal, which can be obtained by subtracting the TA signal of nanotube arrays from that of the hybrid structure, rises a little slower compared with that of pristine aligned nanotube arrays, indicating that the charge transfer process is on the time scale of ~100 fs after deconvolution fitting. The dashed line corresponds to laser cross correlation function.

This journal is © The Royal Society of Chemistry 2019

zero in the next few picoseconds and no time-resolved signal is detected in MoS_2 since the probe photon energy is smaller than the MoS_2 bandgap.[35,36] As for the nanotube-MoS_2 hybrids, the TA signal is enhanced by ~50% compared with that of the pristine nanotube arrays. We attribute the enhanced signal to the interfacial charge transfer: after photoexcitation of MoS_2, both electrons and holes will transfer to the nanotubes due to their type I band alignment.[37,38] The charge transfer signal (Fig. 4g, where the dashed line corresponds to the laser cross correlation function), obtained by subtracting the TA signal of the nanotubes from the hybrid structure, rises a little slower compared with that of pristine nanotubes and reflects that the charge transfer process is ultrafast and on the time scale of only ~100 fs (the fittings are obtained by deconvolution analysis[34]). This ultrafast charge transfer time facilitates the fabrication of fast photoelectric conversion with a speed limit of up to 10 000 GHz.

Conclusions

In conclusion, we have demonstrated a strong-coupled 1D nanotube-2D MoS_2 monolayer hybrid structure through a controlled sequential CVD growth. The post hydrogen annealing before MoS_2 growth is the key to creating a clean interface and the climbing-up growth behaviour of MoS_2 over the nanotubes ensures a large interaction area at the interface, which together lead to strong interfacial coupling both mechanically and electronically. Our work opens up an avenue for assembling low-dimensional materials with controlled interfacial geometry and coupling strength by utilizing complex 2D, 1D and 0D components, therefore it will push the exploration of high-performance device applications of vdW nanomaterials with higher spatial resolution and faster response speed.

Experimental

Carbon nanotube growth

Carbon nanotubes were grown using a CVD method on a 300 nm SiO_2/Si substrate. We used argon bubbled ethanol as a carbon precursor and a thin ion film (0.2 nm) as a catalyst. Before the growth, the catalyst was annealed in air at 700 °C for 5 min, and the system was flushed using ultrahigh purity Ar gas for 10 min. Then, the furnace was ramped to 930 °C with 350 sccm H_2 and 100 sccm Ar passed through ethanol for the synthesis of the nanotubes for 30 min.

Growth of MoS_2 on nanotubes

We grew MoS_2 on nanotubes by atmospheric pressure CVD method using MoO_3 and S powder as precursors. 10 mg of MoO_3 powder was placed at the centre of a tube furnace and 30 mg of S powder at the upstream side, 15 cm from the MoO_3 powder. The substrates with as-grown nanotubes or annealed nanotubes were placed downstream of the position of MoO_3. Before the growth, the system was flushed with ultrahigh-purity Ar gas for 30 min. The temperature of the furnace was then ramped to 750 °C with 15 sccm Ar gas flow for 40 minutes, and then kept at 750 °C with 250 sccm Ar gas flow for 5 min, and then naturally cooled to room temperature with 200 sccm Ar gas.

Optical measurements

Photoluminescence and Raman spectra were recorded using self-built equipment with a laser excitation wavelength of 532 nm. The laser power was set as 1 mW, and the integral time was 1 s for the photoluminescence measurements, 30 s for the Raman measurements. Optical images were taken by an Olympus microscope (Olympus BX51). The pump–probe was measured with femtosecond pulses (~100 fs, 80 MHz) generated by a Ti:sapphire oscillator (Spectra-Physics Mai Tai laser) and an OPO laser. The TA signal, $\Delta R/R = R_{w/pump}/R_{w/o\ pump} - 1$, was recorded using photomultiplier tubes and lock-in amplifier with reflective geometry. More details about the pump–probe setup can be found in our previous work.[34]

Conflicts of interest

The authors declare no conflict of interest.

Acknowledgements

This work was supported by the National Key R&D Program of China (2016YFA0300903 and 2016YFA0300804), the NSFC (11474006 and 51522201), the National Equipment Program of China (ZDYZ2015-1), the Beijing Municipal Science & Technology Commission (Z181100004218006), the Beijing Graphene Innovation Program (Z181100004818003, Z161100002116028), the Bureau of Industry and Information Technology of Shenzhen (No. 201901161512), and the National Postdoctoral Program for Innovative Talents (BX20190016, BX20180013).

References

1 A. K. Geim and I. V. Grigorieva, *Nature*, 2013, **499**, 419–425.
2 C. H. Lee, G. H. Lee, A. M. van der Zande, W. C. Chen, Y. L. Li, M. Y. Han, X. Cui, G. Arefe, C. Nuckolls, T. F. Heinz, J. Guo, J. Hone and P. Kim, *Nat. Nanotechnol.*, 2014, **9**, 676–681.
3 D. Jariwala, T. J. Marks and M. C. Hersam, *Nat. Mater.*, 2017, **16**, 170–181.
4 H. Yang, S. W. Kim, M. Chhowalla and Y. H. Lee, *Nat. Phys.*, 2017, **13**, 931–937.
5 L. Britnell, R. V. Gorbachev, R. Jalil, B. D. Belle, F. Schedin, A. Mishchenko, T. Georgiou, M. I. Katsnelson, L. Eaves, S. V. Morozov, N. M. R. Peres, J. Leist, A. K. Geim, K. S. Novoselov and L. A. Ponomarenko, *Science*, 2012, **335**, 947–950.
6 M. Massicotte, P. Schmidt, F. Vialla, K. G. Schadler, A. Reserbat-Plantey, K. Watanabe, T. Taniguchi,

K. J. Tielrooij and F. H. L. Koppens, *Nat. Nanotechnol.*, 2016, **11**, 42–46.
7 D. Kozawa, A. Carvalho, I. Verzhbitskiy, F. Giustiniano, Y. Miyauchi, S. Mouri, A. H. C. Neto, K. Matsuda and G. Eda, *Nano Lett.*, 2016, **16**, 4087–4093.
8 K. Kang, K. H. Lee, Y. M. Han, H. Gao, S. E. Xie, D. A. Muller and J. Park, *Nature*, 2017, **550**, 229–233.
9 A. G. Kelly, T. Hallam, C. Backes, A. Harvey, A. S. Esmaeily, I. Godwin, J. Coelho, V. Nicolosi, J. Lauth, A. Kulkarni, S. Kinge, L. D. A. Siebbeles, G. S. Duesberg and J. N. Coleman, *Science*, 2017, **356**, 69–72.
10 Z. Y. Lin, Y. Liu, U. Halim, M. N. Ding, Y. Y. Liu, Y. L. Wang, C. C. Jia, P. Chen, X. D. Duan, C. Wang, F. Song, M. F. Li, C. Z. Wan, Y. Huang and X. F. Duan, *Nature*, 2018, **562**, 254–258.
11 C. M. Huang, S. F. Wu, A. M. Sanchez, J. J. P. Peters, R. Beanland, J. S. Ross, P. Rivera, W. Yao, D. H. Cobden and X. D. Xu, *Nat. Mater.*, 2014, **13**, 1096–1101.
12 Y. J. Gong, J. H. Lin, X. L. Wang, G. Shi, S. D. Lei, Z. Lin, X. L. Zou, G. L. Ye, R. Vajtai, B. I. Yakobson, H. Terrones, M. Terrones, B. K. Tay, J. Lou, S. T. Pantelides, Z. Liu, W. Zhou and P. M. Ajayan, *Nat. Mater.*, 2014, **13**, 1135–1142.
13 M. Y. Li, Y. M. Shi, C. C. Cheng, L. S. Lu, Y. C. Lin, H. L. Tang, M. L. Tsai, C. W. Chu, K. H. Wei, J. H. He, W. H. Chang, K. Suenaga and L. J. Li, *Science*, 2015, **349**, 524–528.
14 Z. W. Zhang, P. Chen, X. D. Duan, K. T. Zang, J. Luo and X. F. Duan, *Science*, 2017, **357**, 788–792.
15 J. Zhang, Y. Wei, F. R. Yao, D. Q. Li, H. Ma, P. Lei, H. H. Fang, X. Y. Xiao, Z. X. Lu, J. H. Yang, J. B. Li, L. Y. Jiao, W. D. Hu, K. H. Liu, K. Liu, P. Liu, Q. Q. Li, W. Lu, S. S. Fan and K. L. Jiang, *Adv. Mater.*, 2017, **29**, 1604469.
16 D. Jariwala, V. K. Sangwan, C. C. Wu, P. L. Prabhumirashi, M. L. Geier, T. J. Marks, L. J. Lauhon and M. C. Hersam, *Proc. Natl. Acad. Sci. U. S. A.*, 2013, **110**, 18076–18080.
17 B. Wang, X. L. Li, B. Luo, Y. Y. Jia and L. J. Zhi, *Nanoscale*, 2013, **5**, 1470–1474.
18 L. Sun, W. B. Kong, Y. Jiang, H. C. Wu, K. L. Jiang, J. P. Wang and S. S. Fan, *J. Mater. Chem. A*, 2015, **3**, 5305–5312.
19 Y. P. Liu, X. Y. He, D. Hanlon, A. Harvey, J. N. Coleman and Y. G. Li, *ACS Nano*, 2016, **10**, 8821–8828.
20 D. H. Youn, S. Han, J. Y. Kim, J. Y. Kim, H. Park, S. H. Choi and J. S. Lee, *ACS Nano*, 2014, **8**, 5164–5173.
21 H. L. Huang, W. H. Huang, Z. H. Yang, J. Y. Huang, J. D. Lin, W. P. Liu and Y. J. Liu, *J. Mater. Chem. A*, 2017, **5**, 1558–1566.
22 Y. M. Shi, W. Zhou, A. Y. Lu, W. J. Fang, Y. H. Lee, A. L. Hsu, S. M. Kim, K. K. Kim, H. Y. Yang, L. J. Li, J. C. Idrobo and J. Kong, *Nano Lett.*, 2012, **12**, 2784–2791.
23 A. A. Koos, P. Vancso, G. Z. Magda, Z. Osvath, K. Kertesz, G. Dobrik, C. Hwang, L. Tapaszto and L. P. Biro, *Carbon*, 2016, **105**, 408–415.
24 X. L. Liu, I. Balla, H. Bergeron, G. P. Campbell, M. J. Bedzyk and M. C. Hersam, *ACS Nano*, 2016, **10**, 1067–1075.
25 M. V. Zhao, Y. Ye, Y. M. Han, Y. Xia, H. Y. Zhu, S. Q. Wang, Y. Wang, D. A. Muller and X. Zhang, *Nat. Nanotechnol.*, 2016, **11**, 954–959.
26 L. Ding, A. Tselev, J. Y. Wang, D. N. Yuan, H. B. Chu, T. P. McNicholas, Y. Li and J. Liu, *Nano Lett.*, 2009, **9**, 800–805.
27 J. Liu, C. Wang, X. M. Tu, B. L. Liu, L. Chen, M. Zheng and C. W. Zhou, *Nat. Commun.*, 2012, **3**, 1199.
28 J. T. Wang, T. Y. Li, B. Y. Xia, X. Jin, H. M. Wei, W. Y. Wu, Y. Wei, J. P. Wang, P. Liu, L. N. Zhang, Q. Q. Li, S. S. Fan and K. L. Jiang, *Nano Lett.*, 2014, **14**, 3527–3533.
29 C. Liu and H. M. Cheng, *J. Am. Chem. Soc.*, 2016, **138**, 6690–6698.
30 Y. P. Liao, H. Jiang, N. Wei, P. Laiho, Q. Zhang, S. A. Khan and E. I. Kauppinen, *J. Am. Chem. Soc.*, 2018, **140**, 9797–9800.
31 K. H. Liu, X. P. Hong, M. H. Wu, F. J. Xiao, W. L. Wang, X. D. Bai, J. W. Ager, S. Aloni, A. Zettl, E. G. Wang and F. Wang, *Nat. Commun.*, 2013, **4**, 1375.
32 A. Das, A. K. Sood, A. Govindaraj, A. M. Saitta, M. Lazzeri, F. Mauri and C. N. R. Rao, *Phys. Rev. Lett.*, 2007, **99**, 136803.
33 X. P. Hong, J. Kim, S. F. Shi, Y. Zhang, C. H. Jin, Y. H. Sun, S. Tongay, J. Q. Wu, Y. F. Zhang and F. Wang, *Nat. Nanotechnol.*, 2014, **9**, 682–686.
34 Z. H. Ji, H. Hong, J. Zhang, Q. Zhang, W. Huang, T. Cao, R. X. Qiao, C. Liu, J. Liang, C. H. Jin, L. Y. Jiao, K. B. Shi, S. Meng and K. H. Liu, *ACS Nano*, 2017, **11**, 12020–12026.
35 O. J. Korovyanko, C. X. Sheng, Z. V. Vardeny, A. B. Dalton and R. H. Baughman, *Phys. Rev. Lett.*, 2004, **92**, 017403.
36 H. Y. Shi, R. S. Yan, S. Bertolazzi, J. Brivio, B. Gao, A. Kis, D. Jena, H. G. Xing and L. B. Huang, *ACS Nano*, 2013, **7**, 1072–1080.
37 H. L. Chen, X. W. Wen, J. Zhang, T. M. Wu, Y. J. Gong, X. Zhang, J. T. Yuan, C. Y. Yi, J. Lou, P. M. Ajayan, W. Zhuang, G. Y. Zhang and J. R. Zheng, *Nat. Commun.*, 2016, **7**, 12512.
38 T. Yamaoka, H. E. Lim, S. Koirala, X. F. Wang, K. Shinokita, M. Maruyama, S. Okada, Y. Miyauchi and K. Matsuda, *Adv. Funct. Mater.*, 2018, **28**, 1801021.

This journal is © The Royal Society of Chemistry 2019